Supporting Information

Synergistic sensitization effects of single-atom gold and cerium dopant on mesoporous SnO₂ nanospheres for enhanced volatile sulfur compound sensing

Ping Li[a], Zizheng Wang[a], Youyou Feng[a], Bingxi Feng[a], Dong Cheng[a] and Jing Wei[a]*

[a] Institute of Analytical Chemistry and Instrument for Life Science, The Key Laboratory of Biomedical Information Engineering of Ministry of Education, School of Life Science and Technology, Xi'an Jiaotong University, Xi'an, Shaanxi 710049, P. R. China.

*Corresponding author Jing Wei. E-mail address: jingwei@xjtu.edu.cn

1. The Link

The link to original report of the Japanese cosmetics firm Shiseido for allyl mercaptan as a biomarker: https://corp.shiseido.com/jp/newsimg/2513_i3p50_jp.pdf.

2. Experimental Section

Chemicals. F127 (BioReagent) and $HAuCl_4$ were procured from Sigma-Aldrich. Allyl mercaptan (50%), ethanol (99.7%), methanol (99.5%), ammonia (99.5%), trimethylbenzene (97%), and tannic acid (TA, analytical reagent) were obtained from Macklin Biochemical Co., Ltd. $Ce(NO_3)_3 \cdot 6H_2O$ (99%) and $SnSO_4$, formaldehyde (37-40 wt%) and ammonia (25-28 wt%) were procured from Shanghai Aladdin Reagent Co., Ltd, Meryer Technologies Co., Ltd, respectively. Acetone (99.5%) was bought from Sinopharm Chemical Reagent Co., Ltd.

Preparation of mesoporous Au/Ce-SnO$_2$ nanospheres. F127 (200 mg) was fully dissolved in a mixed solution including water (37 mL), ethanol (8 mL), and ammonia (350 µL). Then, tannic acid (200 mg) and 3.8 mL of formaldehyde solution (3.7 wt%) were added successively. Following 24 h of continuous stirring, the solutions contained $SnSO_4$ (2 mL, 35 mg mL^{-1}), $Ce(NO_3)_3 \cdot 6H_2O$ (15 µL, 48 mg mL^{-1}), and $HAuCl_4$ (33 µL, 0.1 mol L^{-1}) were added. Subsequently, hydrothermal treatment for 12 h was carried out at 100 °C. The resulting Au-Ce-Sn-phenolic colloidal spheres (denoted as Au-Ce-Sn-TA) were obtained and dried at 70 °C. After calcination (400 °C, 3 h), mesoporous SnO_2 nanospheres with single-atom Au and cerium dopant were obtained, which were denoted as Au/Ce-SnO$_2$. For comparison, analogous metal-phenolic colloidal spheres, namely Ce-Sn-TA, Au-Sn-TA, and Sn-TA, were synthesized without Au, Ce, or both precursors. Their derived mesoporous metal oxide spheres were denoted as Ce-SnO$_2$, Au-SnO$_2$, and *meso*SnO$_2$, respectively.

Characterizations. A Gemini SEM500 was employed for capturing scanning electron microscope images, while a Lorenz Transmission Electron Microscope (Talos F200X) was used for obtaining the images of transmission electron microscopy. The nitrogen adsorption-desorption isotherms were obtained using a Micromeritics Tristar 3020 instrument. The Brunauer-Emmett-Teller method was used to calculate the specific surface areas of materials. Pore volumes and pore size distributions were derived from the adsorption branches of isotherms using the Barrett-Joyner-Halenda model. The X-ray diffraction patterns were obtained using a PANalytical X'pertPRO diffractometer. X-ray photoelectron spectroscopy spectra were acquired with a Kratos Axis Ultra DLD. Agilent 5110 was used for the inductively

coupled plasma atomic emission spectroscopy test. The electron paramagnetic resonance was tested in the dark with the help of the German Bruker EMXplus-6/1.

The X-ray absorption spectra including X-ray absorption near-edge structure and extended X-ray absorption fine structure of the samples 4492 eV were collected at the Singapore Synchrotron Light Source center, where a pair of channel-cut Si (111) crystals was used in the monochromator. The storage ring was working at the energy of 800 MeV with average electron current of below 200 mA.

The catalytic products were investigated using Diffuse Reflectance Infrared Fourier Transform Spectroscopy. The material was finely ground and pretreated at 200 °C for 1 h under a nitrogen purge (20 mL min^{-1}). Following this, the temperature was reduced to 125 °C, and a background spectrum was recorded with a resolution of 4 cm^{-1}. After background correction, allyl mercaptan was introduced onto the sample surface at a flow rate of 3 mL min^{-1}.

Electrochemical measurements were conducted at room temperature using an electrochemical workstation (Shanghai CH Instruments, China). Electrochemical measurements including electrochemical impedance spectroscopy and Mott-Schottky analysis, were performed as follows. The reference electrode was Ag/AgCl, the counter electrode was Pt wire, and the working electrode consisted of a glassy carbon substrate with the sample deposited on it. The electrolyte solution contained 0.1 mmol L^{-1} KCl, 10 mmol L^{-1} $K_4Fe(CN)_6 \cdot 3H_2O$, and 10 mmol L^{-1} of $K_3Fe(CN)_6$. The Mott-Schottky plots were measured by using a 0.1 mol L^{-1} Na_2SO_4 solution.

Gas sensing test. MA1.0 tester (Narui Co., LTD.) was used to evaluate the performance of the sensing material on the ceramic tube. Before the test, semiconductor sensing materials (10 mg) were ground into a uniform paste with the help of ethanol (200 μL) and then coated on the surface of the sensor to form a uniform film. The working temperature of the sensor was controlled by adjusting the voltage applied to an ultrafine Ni-Cr alloy coil. To improve the stability of the test, the assembled sensor was aged at 250 °C for 3 days on an aging system before testing.

To demonstrate the exceptional sensing performance of the material, a MEMS sensor was fabricated and tested. The sensing material was finely ground with ultra-pure water to form a homogeneous slurry, which was then carefully applied onto the surface of the central

interfinger electrode of the MEMS chip. After natural drying 1-3 days of the sensing material, the gas-sensitive performance was evaluated using a gas-sensitive analysis system.

A wireless gas device was constructed based on a MEMS sensor. The STM32F103C8T6 core board, HC-06 Bluetooth low energy module, OLED display module, and the prepared MEMS sensor chip were connected to the printed circuit board (PCB) through the female headers. XY-UDT ups and downs power module was connected to the PCB through the female headers to control the operating temperature of the MEMS sensor chip. The remaining components were mounted on the PCB with surface mount technology. All components were placed on the top layer of the PCB. When the test device was turned on, the application-equipped mobile phone can automatically match and connect to the test device's Bluetooth. Once connected, the application will request the test device to acquire and transmit the resistance of the sensor in real-time.

Density Functional Theory calculations. In Density Functional Theory (DFT) calculations, supercells of SnO_2(101) 3×3×1 were constructed. Structural optimizations were performed using the Vienna Ab-initio Simulation Package with a vacuum layer thickness of 25 Å to prevent weak interactions between periodic images. The Perdew-Burke-Ernzerhof functional was employed for exchange-correlation, complemented by DFT-D3 corrections for weak interactions, and a plane-wave basis cut-off energy of 450 eV. k-point sampling was tailored to each supercell type, and self-consistent calculations aimed for a convergence energy threshold of 10^{-5} eV. Adsorption energies of allyl mercaptan on the surface were calculated to understand the interaction effects. Charge density differences were visualized to illustrate the charge distribution resulting from adsorption.
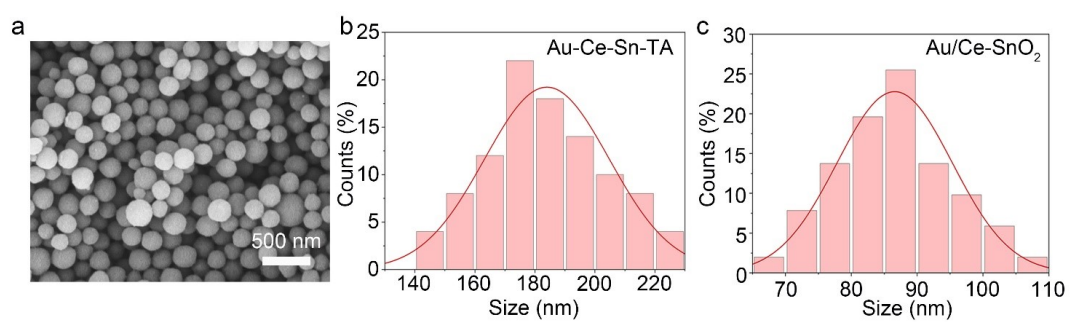
3. Figures

Fig. S1 (a) The SEM image of Au-Ce-Sn-TA. The particle size distribution of (b) Au-Ce-Sn-TA and (c) Au/Ce-SnO$_2$.
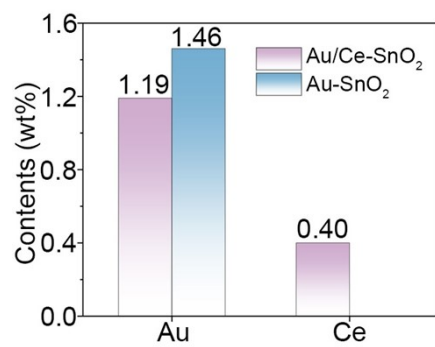
Fig. S2 The inductively coupled plasma atomic emission spectroscopy of the contents of Au and Ce in Au/Ce-SnO$_2$, and Au in Au-SnO$_2$.
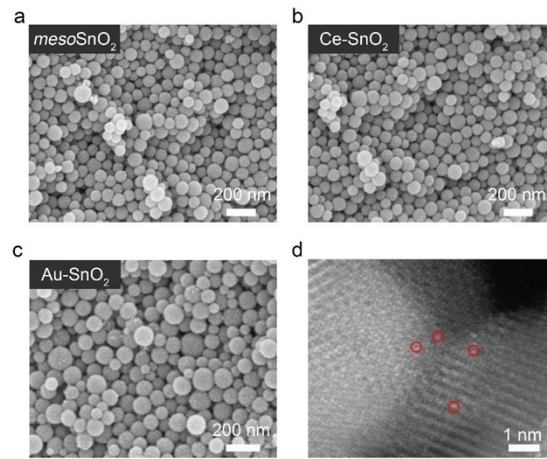
Fig. S3 SEM images of (a) *meso*SnO$_2$, (b) Ce-SnO$_2$, and (c) Au-SnO$_2$. (d) HADDF image for Au-SnO$_2$.
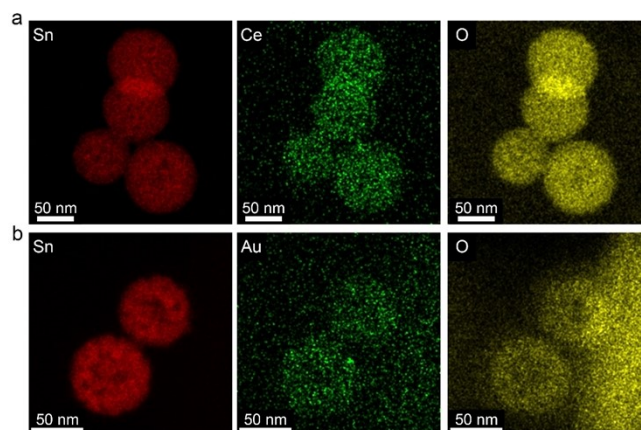
Fig. S4 The element mapping of (a) Ce-SnO$_2$ and (b) Au-SnO$_2$.
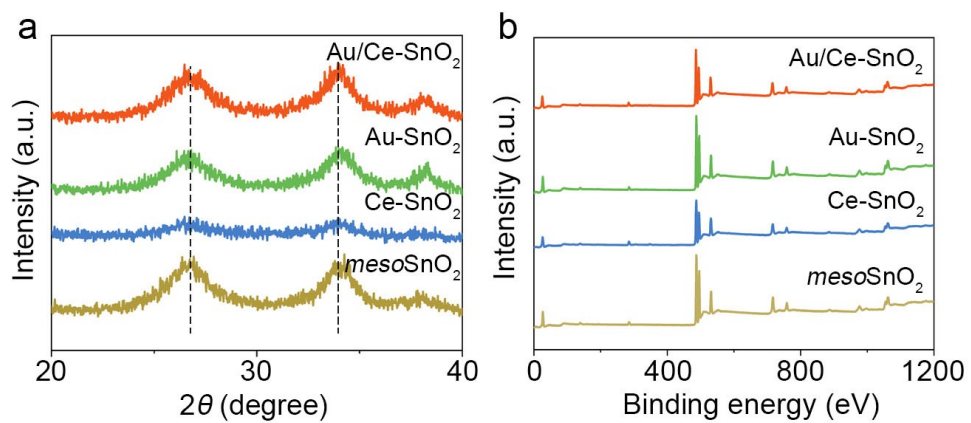
Fig. S5 (a) Partially amplified XRD patterns of Au/Ce-SnO$_2$, Au-SnO$_2$, Ce-SnO$_2$, and *meso*SnO$_2$.

(b) The XPS survey spectrum of Au/Ce-SnO$_2$, Au-SnO$_2$, Ce-SnO$_2$, and *meso*SnO$_2$.
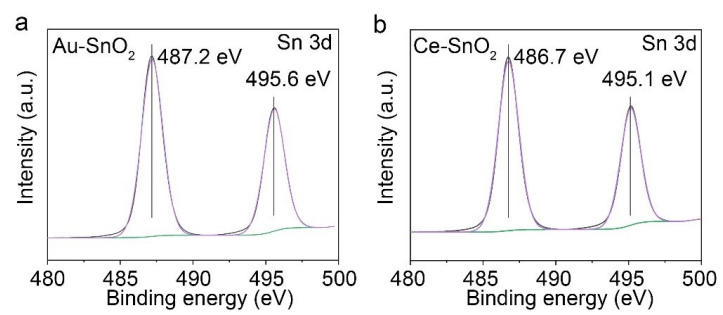
Fig. S6 The Sn 3d spectra of (a) Au-SnO$_2$ and (b) Ce-SnO$_2$.
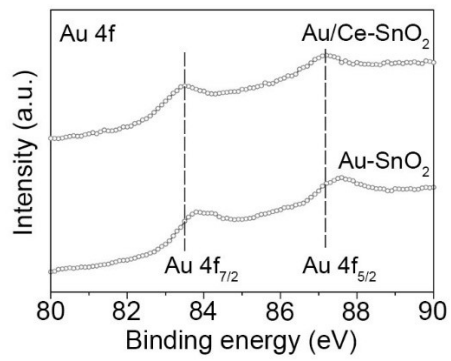
Fig. S7 The Au 4f spectra of Au/Ce-SnO$_2$ and Au-SnO$_2$.
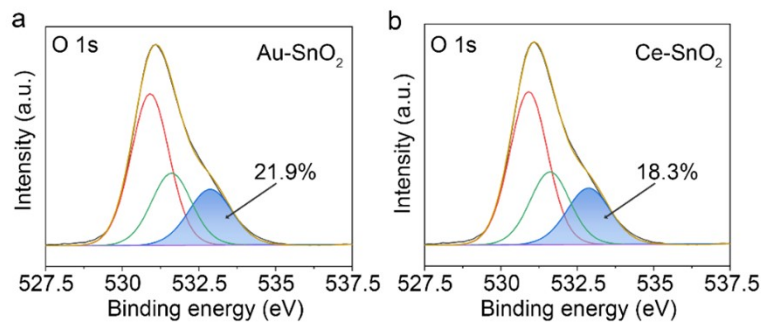
Fig. S8 The O 1s spectra of (a) Au-SnO$_2$ and (b) Ce-SnO$_2$. The proportion in the figure: the percentage of surface adsorbed oxygen.
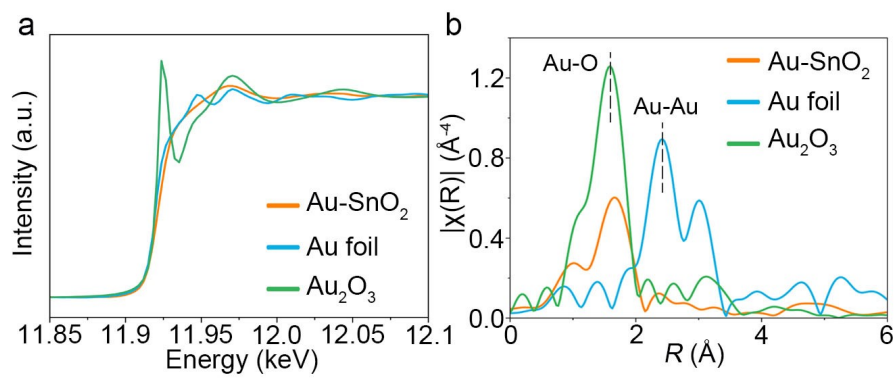
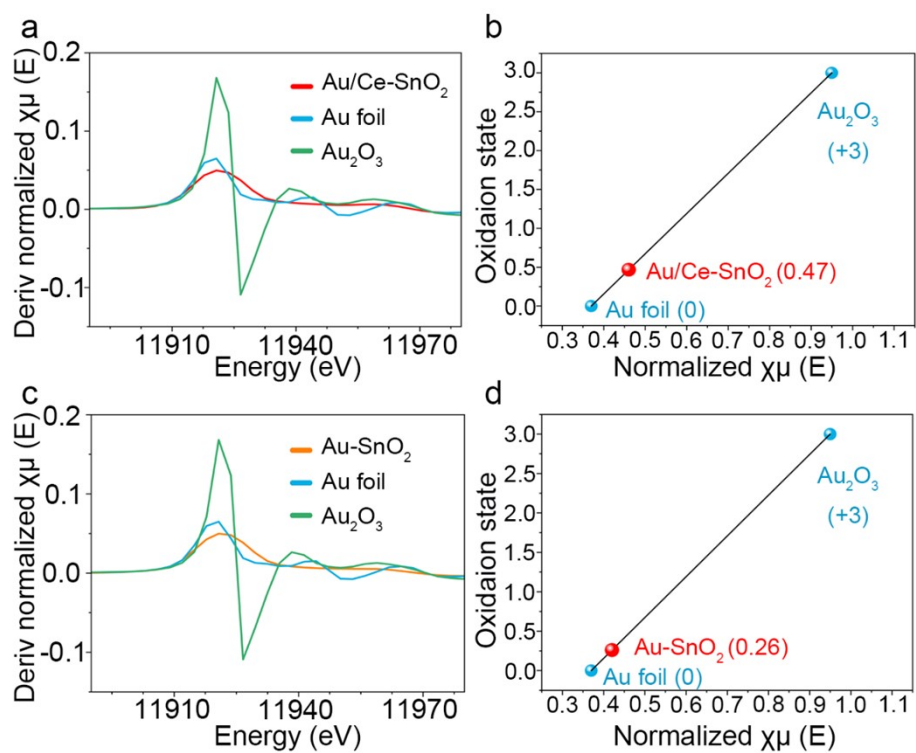**Fig. S9** (a) XANES spectra and (b) EXAFS spectra of Au-SnO$_2$, Au foil, and Au$_2$O$_3$.

Fig. S10 (a) The fitting of Au/Ce-SnO$_2$. (b) The valence state of Au in Au/Ce-SnO$_2$. (c) The fitting of Au-SnO$_2$. (d) The valence state of Au in Au-SnO$_2$.
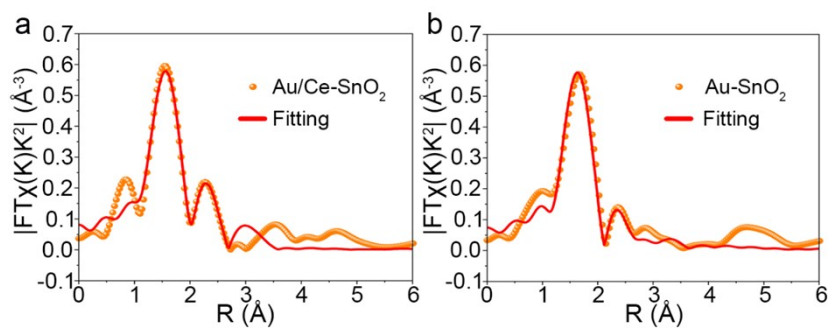
Fig. S11 EXAFS of R-space fitting curves of Au in (a) Au/Ce-SnO$_2$ and (b) Au-SnO$_2$.
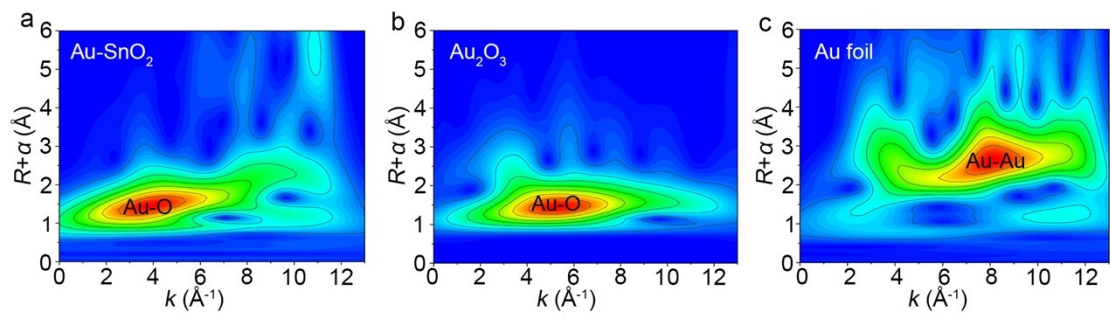
Fig. S12 The wavelet transforms for (a) Au-SnO$_2$, (b) Au$_2$O$_3$, and (c) Au foil.
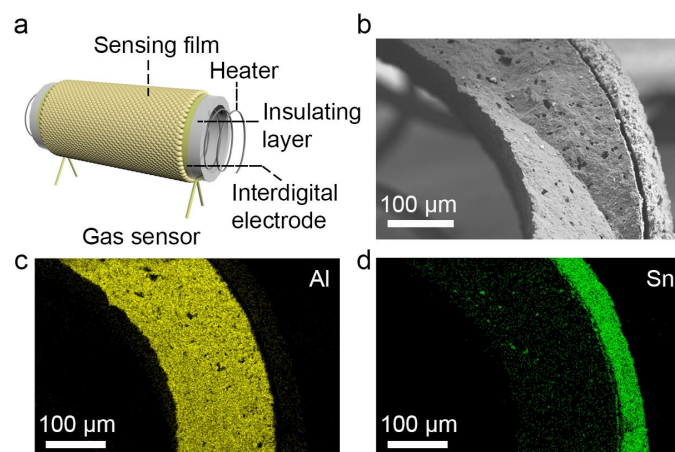
Fig. S13 (a) Schematic diagram of the gas sensor. (b) The SEM of the top view of the sensor. (c) The Al and (d) the Sn mapping of the sensing film.
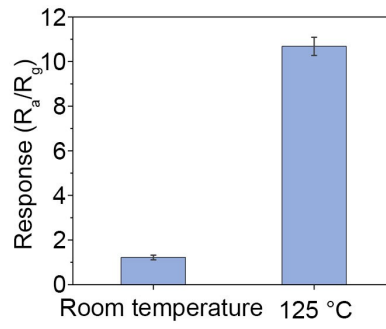
Fig. S14 The response value of Au/Ce-SnO$_2$ sensor for detecting allyl mercaptan at room temperature (25 °C) and 125 °C.
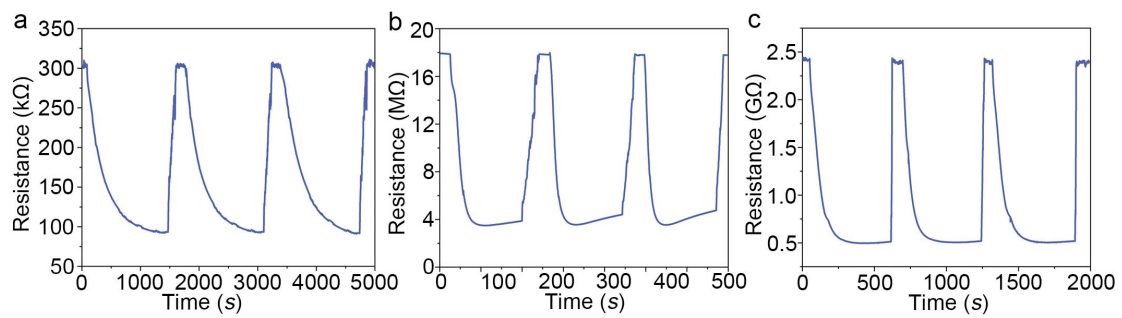
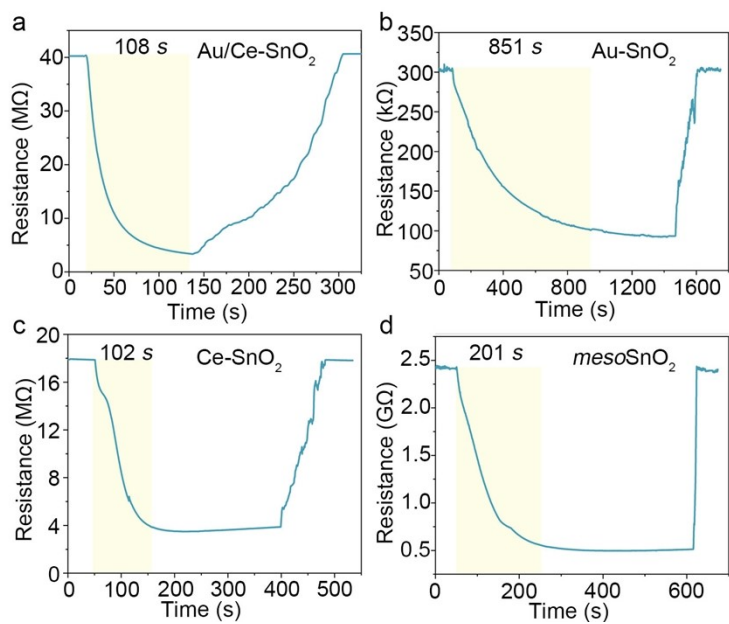**Fig. S15** The response/recovery curves of (a) Au-SnO$_2$, (b) Ce-SnO$_2$, and (c) *meso*SnO$_2$ sensor.

Fig. S16 The response/recovery curve and the response time of (a) Au/Ce-SnO$_2$ and (b) Au-SnO$_2$ sensor at 125 °C, and (c) Ce-SnO$_2$ and (d) *meso*SnO$_2$ sensor at 225 °C.
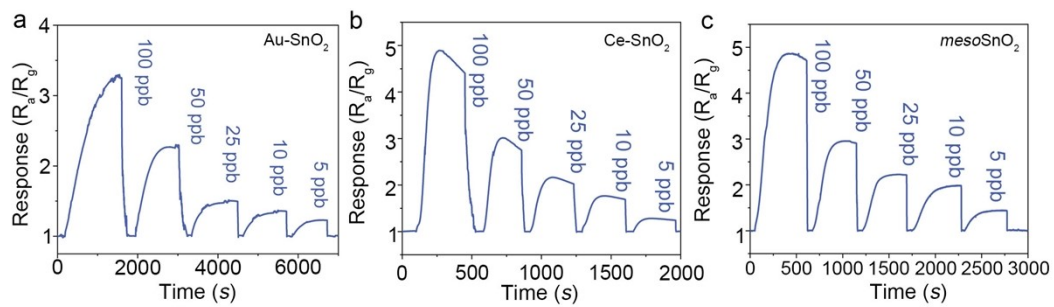
Fig. S17 Dynamic response/recovery curves of (a) Au-SnO$_2$ (125 °C), (b) Ce-SnO$_2$ (225 °C), and (c) *meso*SnO$_2$ (225 °C) sensor.
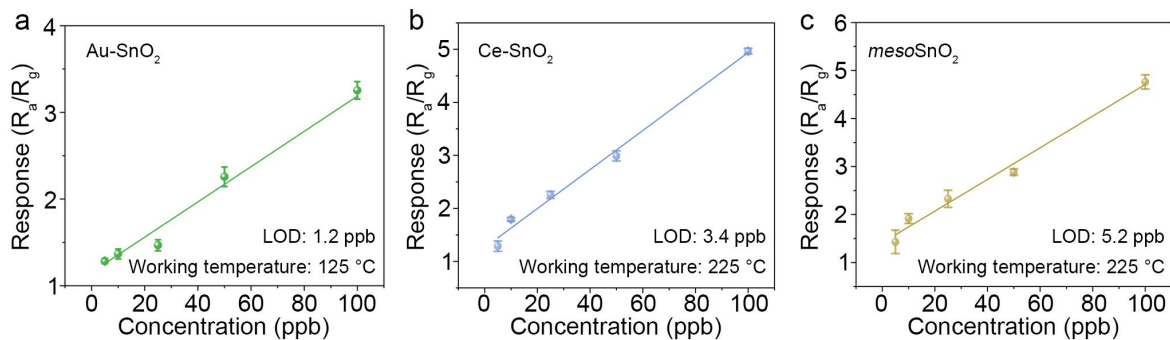
Fig. S18 The response value towards various concentrations (5-100 ppb) of allyl mercaptan with (a) Au-SnO$_2$, (b) Ce-SnO$_2$, and (c) *meso*SnO$_2$ sensor. LOD: limit of detection.
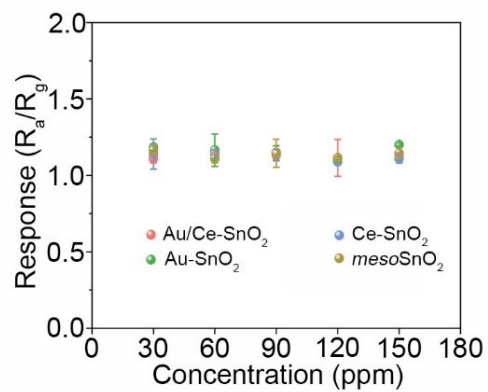
Fig. S19 The response of Au/Ce-SnO$_2$, Au-SnO$_2$, Ce-SnO$_2$, and *meso*SnO$_2$ sensor towards different concentrations of methanol gas (30-150 ppm).
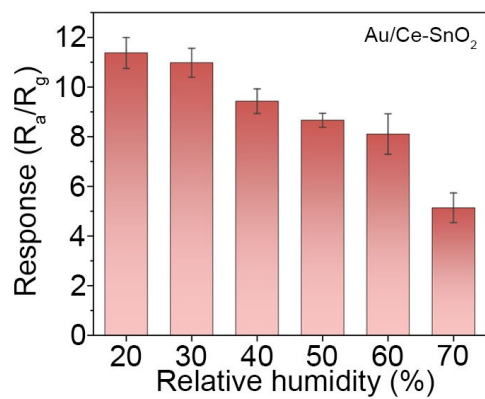
Fig. S20 Relative humidity test (20-70%) for Au/Ce-SnO$_2$ sensor towards 100 ppb allyl mercaptan.
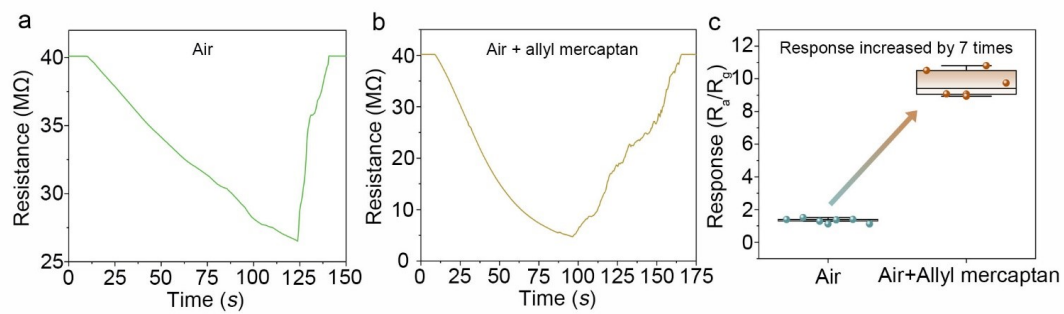
Fig. S21 Actual application simulation results of the response/recovery curves for (a) air and (b) mixed air (air and allyl mercaptan). (c) Actual application simulation results statistics for the leakage monitoring of allyl mercaptan.
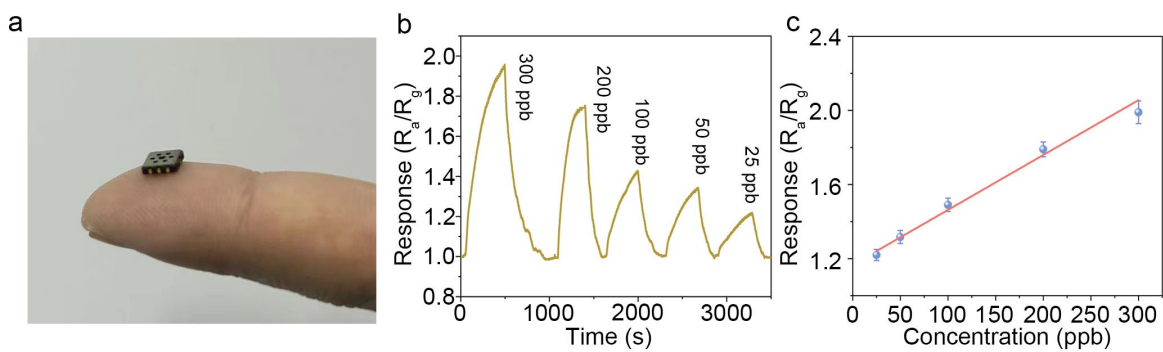
Fig. S22 (a) The digital photo of the MEMS sensor based on Au/Ce-SnO$_2$. (b) The dynamic response/recovery curve and (c) response of the MEMS sensor based on Au/Ce-SnO$_2$ towards different concentrations of allyl mercaptan.
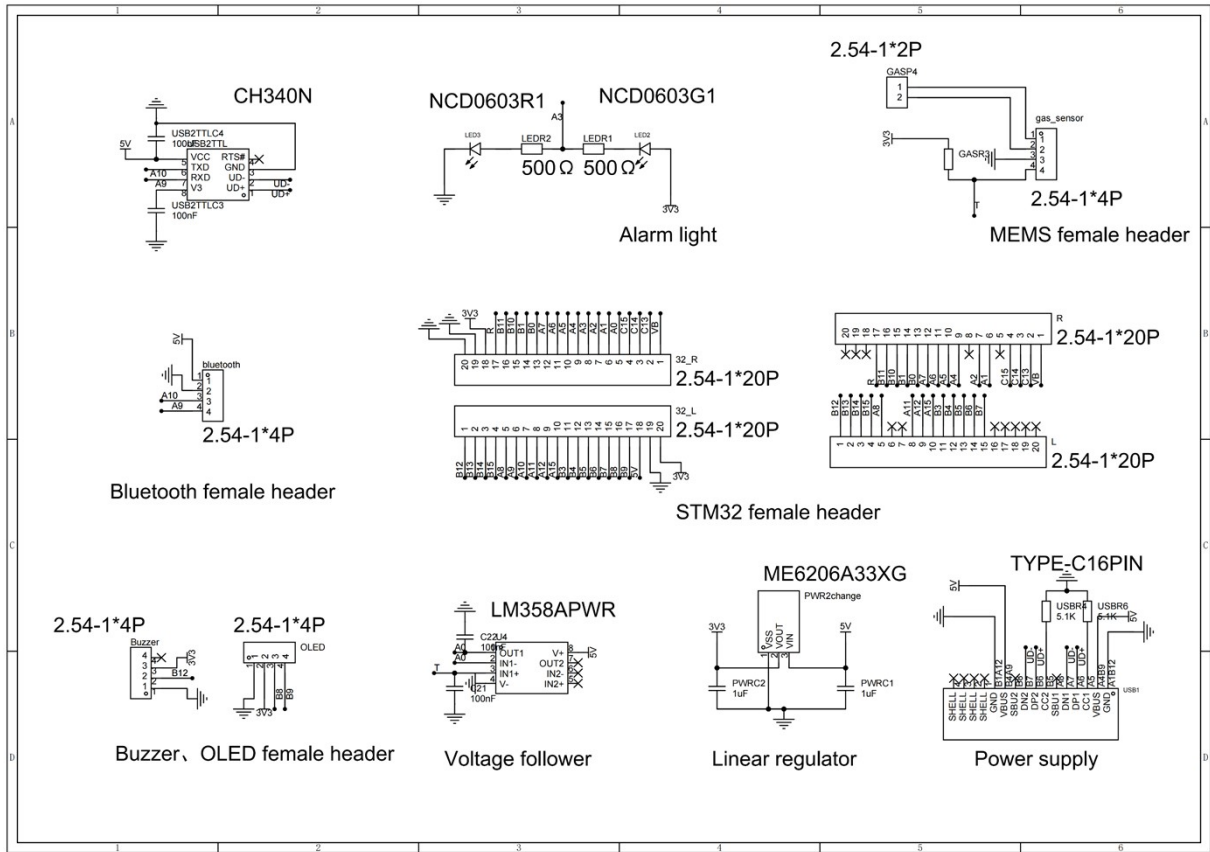
Fig. S23 The circuit diagram of the printed circuit board.
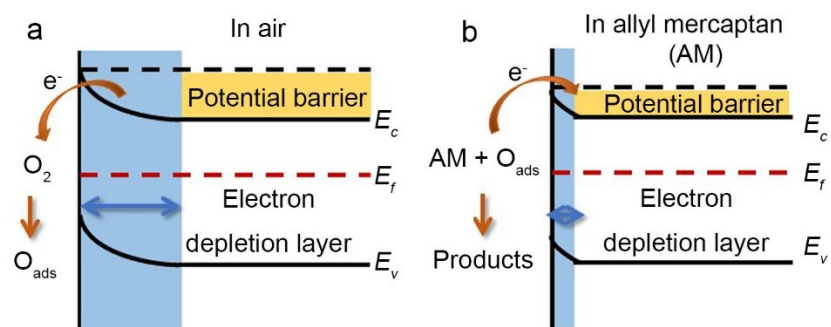
Fig. S24 The electronic structure of Au/Ce-SnO$_2$ (a) in air and (b) in allyl mercaptan (AM). E_c: the conduction band; E_v: the valence band; E_f: the Fermi level of semiconductor; O$_{ads}$: the surface adsorbed oxygen.
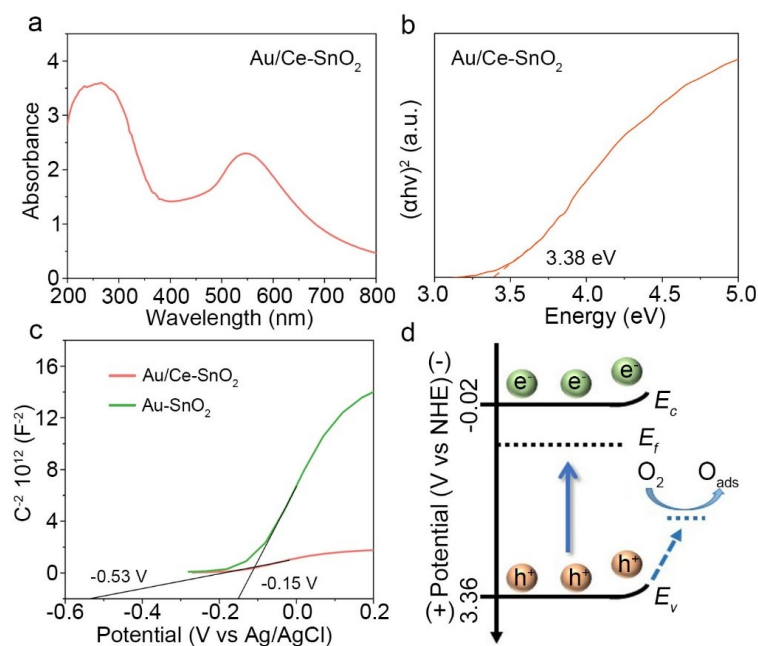
Fig. S25 (a) The diffuse reflection UV-vis absorption spectra and (b) Tauc's plots of Au/Ce-SnO$_2$. (c) The Mott-Schottky plot of Au/Ce-SnO$_2$ and Au-SnO$_2$ materials. (d) The band structure of Au/Ce-SnO$_2$. E_c: the conduction band; E_v: the valence band; E_f: the Fermi level of semiconductor; O$_{ads}$: the surface adsorbed oxygen.

The flat band potential obtained from the extrapolated intercept of the tangent line was -0.53 V vs Ag/AgCl for Au/Ce-SnO$_2$ measured by Mott-Schottky plots. The conduction band (E_c) potential of the n-type semiconductor was usually ≈0.1 V lower than the flat band potential. Hence, the E_c potential of Au/Ce-SnO$_2$ was -0.02 V vs the normal hydrogen electrode (NHE). The bandgap (E_g) for Au/Ce-SnO$_2$ was 3.38 eV, and the valence band (E_v) of Au/Ce-SnO$_2$ was calculated to be 3.36 V.
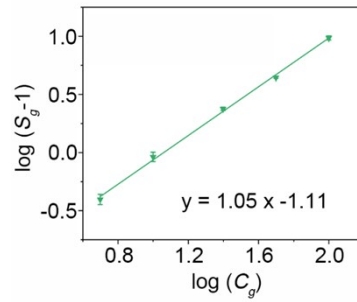
Fig. S26 The ln (|dR|/dt) B 1/T curve of the Au/Ce-SnO$_2$ sensor.

The oxygen ions can be determined by Equation (1) and (2).

$S_g = 1 + AC_g^\beta$ (1)

$\log (S_g - 1) = \log A + \beta \log C_g$ (2)

S_g was the response to the target gas, C_g was the concentration of the target gas, A was a parameter, and β was the surface species charge parameter having a value of 1 for O$^-$ and 0.5 for O^{2-}. The β value of the Au/Ce-SnO$_2$ was close to 1 with the adsorbed oxygen species of O$^-$.
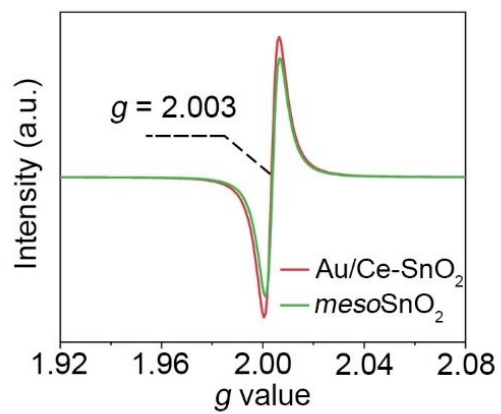
Fig. S27 The electron paramagnetic resonance result for *meso*SnO$_2$ and Au/Ce-SnO$_2$.
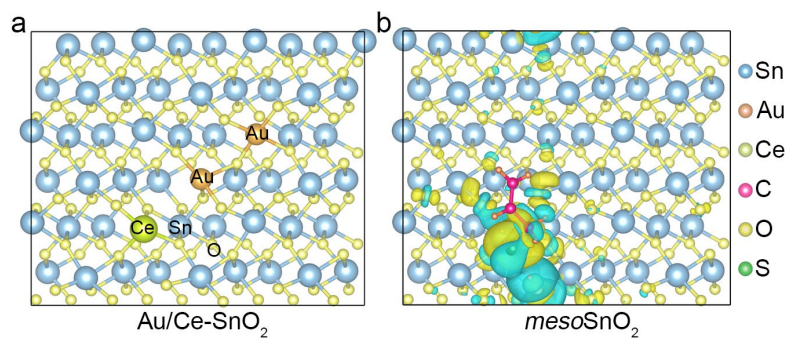
Fig. S28 (a) The optimized adsorption structures of Au/Ce-SnO$_2$ (101). (b) The charge transfer between *meso*SnO$_2$ (101) and allyl mercaptan. The blue region: the consumption of charge; the yellow region: the accumulation of charge.
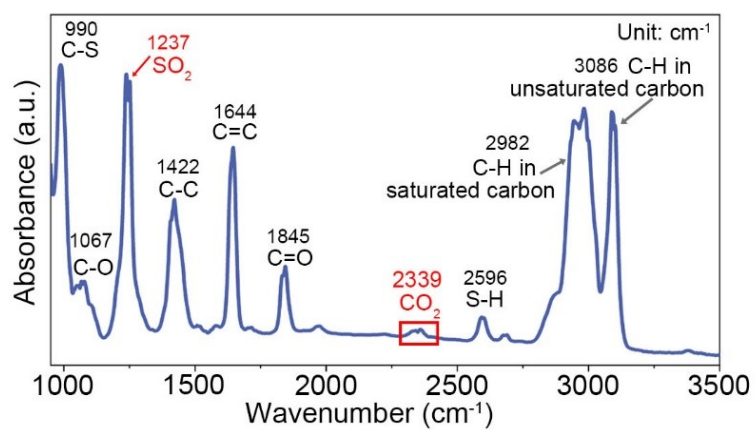
Fig. S29 The diffuse reflectance infrared transform spectroscopy recorded catalysis products on the surface of Au/Ce-SnO$_2$ at 125 °C.

4. Tables

Table S1. The textural properties of Au/Ce-SnO$_2$, Au-SnO$_2$, Ce-SnO$_2$, and *meso*SnO$_2$ materials.

Material	Particle size (nm)	Specific surface area (m^2 g^{-1})	Pore size (nm)
Au/Ce-SnO$_2$	86	89.4	5.8
Au-SnO$_2$	70	83.2	5.8
Ce-SnO$_2$	72	81.5	5.8
*meso*SnO$_2$	88	78.6	5.8

Table S2. Fitting results of Ce 3d XPS spectra of Au/Ce-SnO$_2$ and Ce-SnO$_2$ materials.

Material	Ce species	Binding energy (eV)	Percentage (%)
Au/Ce-SnO$_2$	Ce(III)	886.2, 905.0	46.5
Au/Ce-SnO$_2$	Ce(IV)	882.8, 889.9, 900.6	53.5
Ce-SnO$_2$	Ce(III)	885.7, 904.5	48.0
Ce-SnO$_2$	Ce(IV)	882.1, 889.3, 904.5	52.0

Table S3. Fitting results of O 1s XPS spectra of Au/Ce-SnO$_2$, Au-SnO$_2$, Ce-SnO$_2$, and *meso*SnO$_2$ materials.

Material	Oxygen species	Binding energy (eV)	Percentage (%)
Au/Ce-SnO$_2$	O$_L$	530.35	45.1
Au/Ce-SnO$_2$	O$_v$	531.19	31.5
Au/Ce-SnO$_2$	O$_c$	532.51	23.4
Au-SnO$_2$	O$_L$	530.91	52.1
Au-SnO$_2$	O$_v$	531.60	26.0
Au-SnO$_2$	O$_c$	532.87	21.9
Ce-SnO$_2$	O$_L$	530.49	53.8
Ce-SnO$_2$	O$_v$	531.58	27.9
Ce-SnO$_2$	O$_c$	532.74	18.3
*meso*SnO$_2$	O$_L$	530.91	59.9
*meso*SnO$_2$	O$_v$	531.87	25.1
*meso*SnO$_2$	O$_c$	532.98	15.0

O$_L$: Lattice oxygen; O$_V$: Oxygen vacancies; O$_C$: Surface adsorbed oxygen.

Table S4. EXAFS fitting parameters at the Au L3-edge for various samples.

Sample	Shell	CN	R(Å)	σ^2(Å^2)	ΔE_0(eV)	R factor
Au foil	Au-Au	12.0	2.76±0.013	0.0073	4.3	0.0042
Au_2O_3	Au-O	4.4±0.3	1.98±0.01	0.0028	8.0	0.0087
Au/Ce-SnO$_2$	Au-O	2.2±0.1	2.02±0.01	0.0055	11.7	0.0085
Au-SnO$_2$	Au-O	1.9±0.1	2.06±0.01	0.0022	14.2	0.0171

CN: Coordination number; R: The distance between absorber and backscatter atoms; σ^2: Debye-Waller factor to account for both thermal and structural disorders; ΔE_0: Inner potential correction; R factor: The goodness of the fit.

Table S5. The sensing performance of Au/Ce-SnO$_2$, Au-SnO$_2$, Ce-SnO$_2$, and *meso*SnO$_2$ sensors for detecting allyl mercaptan.

Gas sensor	Temperature (°C)	Concentration (ppm)	Response	LOD (ppb)	Sensitivity (ppb^{-1})	Reference
Porous NiO nanosheets	225	40	56.7[a]	15[c]	0.000256	1
MnO$_2$@NiO nanosheets	275	12	9.7[a]	32[c]	0.0000549	1
CeO$_2$ nanoparticle /SnO$_2$ nanosheet	550	54	33[b]	11000[d]	-	2
SnO$_2$ nanosheet	550	54	3.2[b]	11000[d]	-	2
*meso*SnO$_2$ nanospheres	225	0.1	4.7[b]	5.2[c]	0.032	**This work**
Ce-SnO$_2$ nanospheres	225	0.1	4.9[b]	3.4[c]	0.037	**This work**
Au-SnO$_2$ nanospheres	125	0.1	3.3[b]	1.2[c]	0.021	**This work**
Au/Ce-SnO$_2$ nanospheres	125	0.1	10.7[b]	0.74[c]	0.097	**This work**

LOD: Limit of detection.

a): R_g/R_a; b) R_a/R_g. R_g and R_a are the resistances of sensors in target gas and air, respectively.

c): Calculated LOD; d): Experimental LOD.

References

1   C. Li, P. G. Choi and Y. Masuda, *Adv. Sci.*, 2022, **9**, 2202442.

2   T. Ema, P. G. Choi, S. Takami and Y. Masuda, *ACS Appl. Mater. Interfaces*, 2022, **14**, 56998-57007.